# A General Method of Fabricating Flexible Spinel-Type Oxide/Reduced Graphene Oxide Nanocomposite Aerogels as Advanced Anodes for Lithium-Ion Batteries

Guobo Zeng,[†] Nan Shi,[‡] Michael Hess,[§] Xi Chen,[†] Wei Cheng,[†] Tongxiang Fan,[‡] and Markus Niederberger*,[†]

[†]Laboratory for Multifunctional Materials, Department of Materials, ETH Zurich, Vladimir-Prelog-Weg 5, 8093, Zurich, Switzerland, [‡]State Key Laboratory of Metal Matrix Composites, Department of Materials Science and Engineering, Shanghai Jiao Tong University, Shanghai, 200240, PR China, and [§]Institute of Inorganic Chemistry, Department of Chemistry and Applied Biosciences, ETH Zurich, Vladimir-Prelog-Weg 1, 8093, Zurich, Switzerland

ABSTRACT High-capacity anode materials for lithium ion batteries (LIBs), such as spinel-type metal oxides, generally suffer from poor Li^+ and e^- conductivities. Their drastic crystal structure and volume changes, as a result of the conversion reaction mechanism with Li, severely impede the high-rate and cyclability performance toward their practical application. In this article, we present a general and facile approach to fabricate flexible spinel-type oxide/ reduced graphene oxide (rGO) composite aerogels as binder-free anodes where the spinel nanoparticles (NPs) are integrated in an

interconnected rGO network. Benefiting from the hierarchical porosity, conductive network and mechanical stability constructed by interpenetrated rGO layers, and from the pillar effect of NPs in between rGO sheets, the hybrid system synergistically enhances the intrinsic properties of each component, yet is robust and flexible. Consequently, the spinel/rGO composite aerogels demonstrate greatly enhanced rate capability and long-term stability without obvious capacity fading for 1000 cycles at high rates of up to 4.5 A g^{-1} in the case of $CoFe_2O_4$. This electrode design can successfully be applied to several other spinel ferrites such as $MnFe_2O_4$, Fe_3O_4, $NiFe_2O_4$ or Co_3O_4, all of which lead to excellent electrochemical performances.
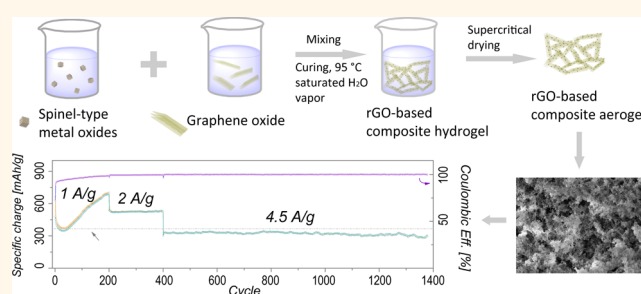
KEYWORDS: nanocomposites · spinel nanocrystals · graphene oxide · flexible aerogels · Li-ion batteries

Technological improvements in lithium-ion batteries (LIBs) are driven by an ever-increasing demand for portable electronic devices and electric vehicle applications.[1] The main challenge remains in developing electrode materials with higher capacity, faster rate performance and longer lifespan.[2,3] Higher capacity means more Li uptake per transition metal or carbon, thus a larger change in the oxidation state is associated with the transition metal. As a result, the mechanism changes from classical intercalation, as in the case of, *e.g.*, C/LiC$_6$ or Li$_4$Ti$_5$O$_{12}$/Li$_7$Ti$_5$O$_{12}$, to conversion (*e.g.*, Co$_3$O$_4$/Co), and alloying (*e.g.*, Sn/Li$_{4.4}$Sn). Besides metal oxides, transitional metal sulfides (*e.g.*, MoS$_2$) also show promise as conversion-type

materials for LIB applications.[4,5] In sharp contrast to interlayer/interstitial Li insertion with only small or even zero strain, an abrupt structural change takes place upon electrode discharging for metal oxides/sulfides undergoing conversion, *e.g.*, reaction of Co$_3$O$_4$ to metallic Co and formation of Li$_2$O.[6,7] Consequently, high-energy density anodes suffer from mechanical degradation due to lithiation-induced volume expansion, electrode pulverization and detachment from the conducting environment during long-term cycling, resulting in large irreversible capacity loss, low Coulombic efficiency and poor cycling stability. In addition, low Li^+ and e^- conductivities are generally associated with metal oxides, which limits the high-rate performance.[8] Many
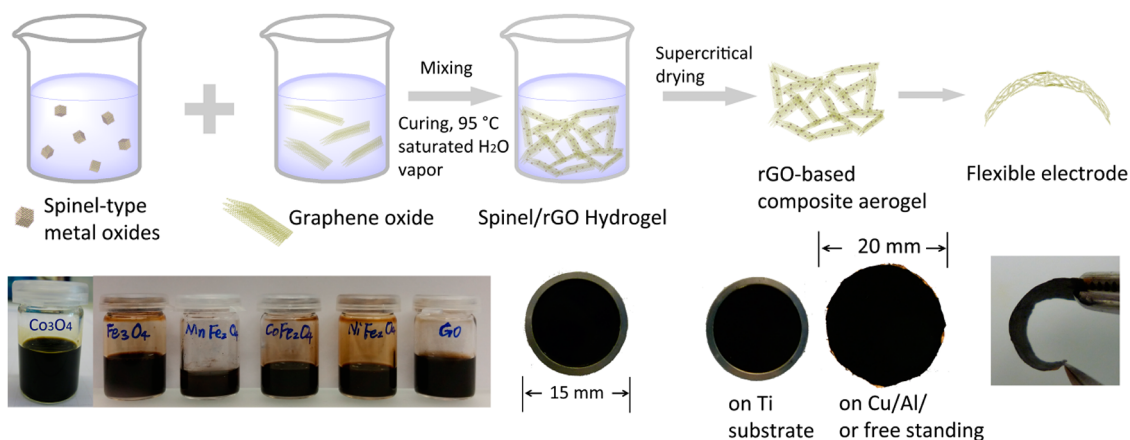
Scheme 1. Schematic illustration of the fabrication process for spinel/rGO nanocomposite aerogel films. Colloidally stable spinel-type NPs and GO dispersions are used as building blocks. The combined suspension is cured under a saturated H_2O vapor environment at 95 °C for 6 h, leading to a monolithic gel film. After supercritical drying, a flexible rGO-based composite aerogel with a rationally controlled shape is obtained. The free standing aerogel films can be bent without breaking.

attempts to tackle these issues have been focused on nanosizing the materials,[9] e.g., by preparing nanoparticles (NPs), nanowires, or nanotubes, owing to their enhanced electrode kinetics. However, reduction of the particle size alone cannot prevent severe capacity fading upon prolonged high-rate cycling due to drastic volume changes coming along with the conversion/alloying reaction. This problem can be addressed by the preparation of carbon-based nanocomposites.[7,10−13] For example, graphene decorated with Co_3O_4 NPs presented enhanced reversible capacity and cyclic performance as anode for LIBs.[7] In spite of all this progress, there is still much room to improve the reversible capacity, the Coulombic efficiency, and the cycle life with good rate capability of conversion-type electrode materials. The optimization of the three-dimensional (3D) electrode architecture has been recognized as critical on the way to achieve superior performance of LIBs, particularly with hierarchical porous electrodes.[8] For example, Yi et al. proposed a pomegranate-like Si−C hybrid electrode with a nano-scale design in which each single Si particle was encapsulated in a spacious hollow carbon shell to leave enough room for expansion upon Li uptake, leading to extraordinary cyclability.[14] The key to success is the presence of enough void space or porosity in the electrode, which facilitates electrolyte diffusion while maintaining good electron transport and accommodating large volume changes.

Nowadays, there is also growing interest in light-weight and flexible LIBs to meet the special needs for high-performance and flexible electronics, such as wearable devices or implantable biomedical devices.[3,15] However, to fabricate a flexible electrode with high-efficiency additional requirements have to be considered. The appropriate, often nanoscale, electrode material and the electrode architecture have to be engineered into a robust, but yet flexible form. Mesoporous carbon-based materials, graphene or carbon

nanotubes are preferred candidates to be integrated with active materials owing to their high e− conductivity and excellent mechanical stability.[16−19] For instance, Cheng et al. built a flexible hybrid electrode based on a 3D porous graphene framework via a template-assisted CVD procedure, which finally resulted in outstanding electrochemical (EC) performance.[3] To build up hierarchical porosity generally sophisticated techniques, such as soft/hard templating, followed by acid etching or heat treatment, are usually required.

Here we present a simple and general method to fabricate flexible reduced graphene oxide (rGO)−spinel-type metal oxide nanoparticle (NP) aerogel composites as advanced anodes overcoming several of the limitations discussed before. A monolith of rGO-based composite aerogel with embedded spinel-type metal oxide nanoparticles was designed and directly used as binder-free anode. The interconnected rGO sheets offer a hierarchical porosity, and the introduction of NPs as spacers/pillars between the rGO interlayers plays a critical role to prevent the hierarchical structure from collapsing. As a result of this architecture, synergistic effects are expected to lead to high capacity and long-term cycling stability of the electrode.

RESULTS AND DISCUSSION

The fabrication protocol of rGO-based composite aerogels is simple, as shown in Scheme 1. First, colloidally stable NP suspensions are needed, which can be obtained through tailoring the surface chemistry, in this case by tuning the surface charge to be positive. The positively charged metal oxide NPs can then be intimately mixed with aqueous dispersions of negatively charged GO. In addition to electrostatic attraction between the two building blocks, $\pi−\pi$ interactions between the GO sheets support the self-assembly process. Upon gelling in a mold at 95 °C, the NPs are homogeneously integrated into the interconnected
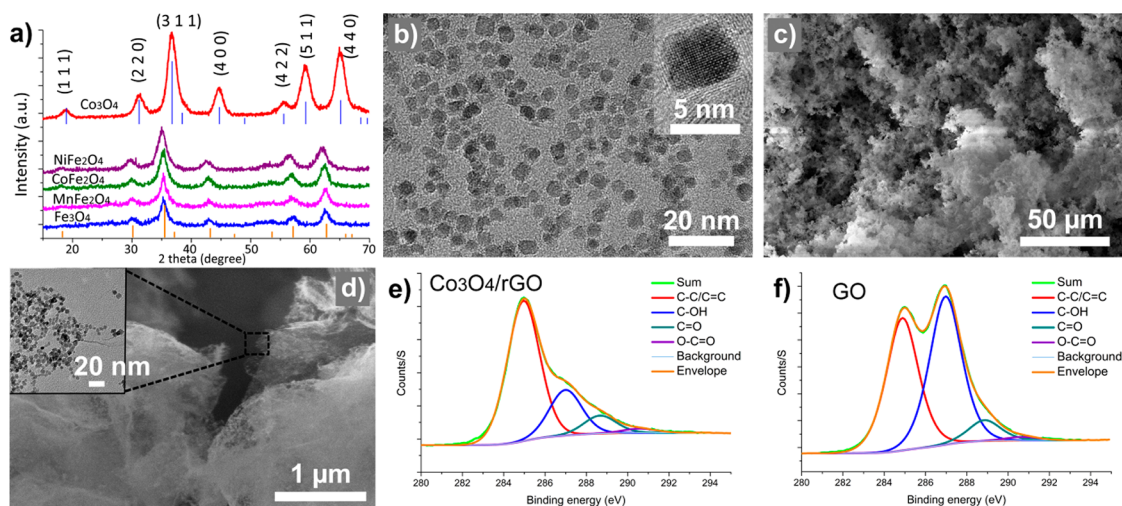
Figure 1. (a) XRD patterns for all the as-prepared spinel-type transition metal oxides. (b) TEM image of the Co_3O_4 nanocrystals with cube-like morphology and narrow particle size distribution (inset: HRTEM of a Co_3O_4 nanocube). (c) SEM image of the Co_3O_4/rGO composite aerogel at low magnification, and (d) at higher magnification (inset: TEM image of the composite aerogel, showing that the Co_3O_4 nanocrystals are homogeneously distributed and intimately anchored on the rGO sheets). (e) High resolution XPS spectra of C 1s for the Co_3O_4/rGO aerogel and (f) the pristine GO sample, giving evidence for the partial reduction of the GO in the composite sample.

rGO network, forming a monolithic hydrogel. As already reported before for nanoparticle-based metal oxide aerogels,[20−22] it is critical to carefully tune the different interactions between the building blocks to get an efficient gelling process. After supercritical drying, a crack-free and flexible aerogel film (minimum ~100 μm in thickness) was obtained, which was directly used as the electrode without any further additives. The shape of the as-obtained composite aerogels is dependent on the shape of the containers and the substrates. A film or a bulk composite aerogel can be made on different substrates, e.g., Ti, Cu, Al, or even a free-standing one can be produced if a Teflon container is used (details can be found in the Experimental Section). The interconnections of the graphene sheets offer enough mechanical strength and flexibility, so that the composite aerogel film can be bent or twisted without breaking.

This modular approach starting from preformed building blocks is rather different to other GO based composite aerogel preparation routes, where typically the NPs are hydro- or solvothermally grown on GO from molecular precursors.[23−26] This seemingly small experimental detail has a profound effect on the electrode preparation. In the latter case, the as-synthesized powders have to be processed into the electrodes by grinding/milling with binder, typically resulting in electrodes with lower porosity, and thus limited improvement in EC performance. In our case, the composite aerogel is directly assembled in the desired electrode geometry, preventing the use of binders and thus giving access to electrodes with high porosity and good mechanical flexibility.

To achieve high homogeneity at the nanoscale in the final composite, colloidally stable NP suspensions

are the prerequisite. For this purpose, we developed a novel synthesis route for Co_3O_4 NPs, where Co(II) acetate was dissolved into a mixture of benzyl alcohol and ammonia solution, followed by heating in an oil bath at 165 °C for 2 h. After rinsing and drying, a black powder was obtained, which could be identified by powder X-ray diffraction (XRD) as Co_3O_4 (ICDD PDF No. 01−073−1701, Figure 1a). The broad reflections are characteristic for small nanocrystals. The crystallite sizes are estimated to be 5 nm calculated from the (4 0 0) and (4 4 0) reflections using the Scherrer equation, which is consistent with the results from transmission electron microscopy (TEM) as depicted in Figure 1b. The Co_3O_4 NPs exhibit a cube-like morphology, a low degree of agglomeration and a narrow particle size distribution with an average size of 4.6 nm. Because of the positive charge on the surface, as confirmed by the ζ-potential measurement (Table 1), the Co_3O_4 NPs can be dispersed into H_2O at high concentrations up to 30 mg/mL without any surfactants, and they are stable for several weeks (Scheme 1). The other spinel-type ferrites (MFe_2O_4, M = Mn, Fe, Co and Ni) were prepared by a slightly modified microwave-assisted benzyl alcohol route reported before.[27] The respective metal organic precursors and a small amount of ethylenediamine were dissolved in benzyl alcohol and heated at 195 °C for a few minutes under microwave irradiation. The NPs were identified by XRD as Fe_3O_4 (ICDD PDF No. 00−01−1111), $MnFe_2O_4$ (No. 00−10−0319), $CoFe_2O_4$ (No. 00−01−1121), and $NiFe_2O_4$ (No. 00−03−0875), respectively. The as-obtained ferrites display similar cube-like morphology like the Co_3O_4 NPs, however with a broader size distribution (Figure S1, Supporting Information). But in contrast to cobalt oxide, the as-obtained ferrites could

TABLE 1. ζ-Potentials for the Colloidal NP Suspensions

	Co_3O_4	$MnFe_2O_4$	Fe_3O_4	$CoFe_2O_4$	$NiFe_2O_4$	GO
ζ-potential (mV)	38.7	21.5	40.5	26.0	21.4	−24.8
conductivity (mS/cm)	0.1151	0.4887	0.2936	0.3966	0.3480	1.0179

not be well dispersed in H_2O in the required high concentrations. Therefore, 2-(2-(2-methoxyethoxy)ethoxy)acetic acid, MEEAA, was added to increase the stability of the aqueous dispersions. All the NPs are positively charged after the surface functionalization as confirmed by the ζ-potential measurement (Table 1). In the end, colloidally stable suspensions were obtained for all the ferrite NPs, except for $MnFe_2O_4$, which continued to have some tendency to agglomerate.

During the curing step, the GO sheets start to cross-link and self-assemble into a macroscopic gel. The positive surface charge of the NPs enables intimate binding to the negatively charged GO sheets, resulting in a large number of NPs uniformly incorporated into the interconnected GO network. The obtained wet gels exhibit disordered and open macroporosity which is clearly visible on the SEM image. As a representative example, the morphology of Co_3O_4/rGO composite aerogel is shown in Figure 1c. SEM images of all the other spinel/rGO composite aerogels and of the pure rGO aerogel without NPs can be found in the Figure S2. The SEM image at higher magnification (Figure 1d) shows that the GO sheets are corrugated with abundant NPs embedded between them. The inset TEM image reveals more clearly that plenty of Co_3O_4 NPs are homogeneously distributed on the rGO sheets. The specific surface area and the porosity were characterized by nitrogen adsorption−desorption isotherm measurements for the Co_3O_4/rGO composite aerogel and for the rGO aerogel without nanoparticles (Figure S3−S4). The rGO aerogel possesses remarkably high BET specific surface area of up to 815 m^2 g^{-1}. For the Co_3O_4/rGO aerogel the surface area is 332 m^2 g^{-1} due to the large amount of heavy Co_3O_4 nanocrystals. The pore size distribution further demonstrates the existence of some mesoporosity between 3 and 40 nm.

Interestingly, X-ray photoelectron spectroscopy (XPS) measurements show that the GO is partially reduced even under the mild treatment conditions of 95 °C. As an example, Figure 1e and 1f depict the C 1s XPS high resolution spectra on the composite Co_3O_4/GO sample and the pristine GO sample, respectively. The envelope of the C 1s peak is deconvoluted into four components,[28] corresponding to C—C/C=C (aromatic rings, 284.9 eV), C—OX (epoxy (X = C) and hydroxyl groups (X = H), 287.0 eV), C=O (288.7 eV) and O—C=O (carboxyl groups, 290.6 eV). Comparing the spectra, we can clearly observe that the signal attributed to the C—OH groups is significantly decreased for the heat treated sample. This observation indicates that oxygen-containing functional groups on

the GO sheets are partially removed upon thermal treatment, which is beneficial for the electronic conductivity.[29] Other samples display similar results that can be found in Figure S5.

The use of nanostructured composite aerogels as electrode materials represents a promising avenue to boost the electrochemical performance, as this strategy synergistically strengthens the advantages of each component, but also mitigates their disadvantages.[8,30] In our study, we chose spinel-type transition metal oxides as demonstration anodes as they can offer high theoretical capacity *via* conversion mechanism. However, problems generally associated with conversion-type materials such as abrupt structure and volume changes upon cycling and unfavorable e$^-$ and Li$^+$ conductivity also apply to spinels. Consequently, poor cyclability (less than 150 cycles) is a general issue for most of the reported results.[7,10−13] On the other hand, graphene or graphene oxide received broad attention in energy storage applications due to its high specific surface area and e$^-$ conductivity. It can store Li$^+$ *via* a double-sided adsorption mechanism forming LiC$_3$ with a theoretic specific charge of 744 mAh g^{-1}, which is double of the theoretical capacity of 372 mAh g^{-1} for graphite.[31] Unfortunately, graphene is prone to re-stacking, leading to drastic fading in its high initial capacities. To address these issues and to exploit high performance electrodes, we designed a rGO-based composite aerogel with embedded spinel-type metal oxide nanoparticles. rGO based aerogels can offer a hierarchical porosity, in which the macropores act as a buffering reservoir for the Li-ion containing electrolyte, facilitating the diffusion to the interior surfaces, while the mesopores provide a large accessible surface area for the Li$^+$ transport/storage and accommodate any local volume changes upon Li$^+$ insertion/extraction for conversion-type metal oxides.[32] The introduction of NPs as spacers/pillars between graphene or rGO interlayers plays a critical role to prevent the hierarchical structure from collapsing. In return, the rGO sheath protects the NPs from detaching from the conducting medium, and its percolating graphitic network provides a conductive pathway for e$^-$ transport for the active NPs. As a result of this design, synergistic effects are expected to lead to high capacity and long-term cycling stability of the electrode.

To demonstrate the benefits of the composite electrode with the hierarchical microstructure, the Co_3O_4/rGO and $CoFe_2O_4$/rGO aerogel films are discussed as examples in more details. Data from the other composites ($MnFe_2O_4$, Fe_3O_4, and $NiFe_2O_4$) are included in the Supporting Information (Figure S6−S9). A constant voltage (CV, potentiostatic) step after the constant current mode (CC, galvanostatic) helps to complete discharge/charge, particularly at high current rate. In order to study the kinetic behaviors of Li$^+$ insertion/removal into/from the composite electrodes at different
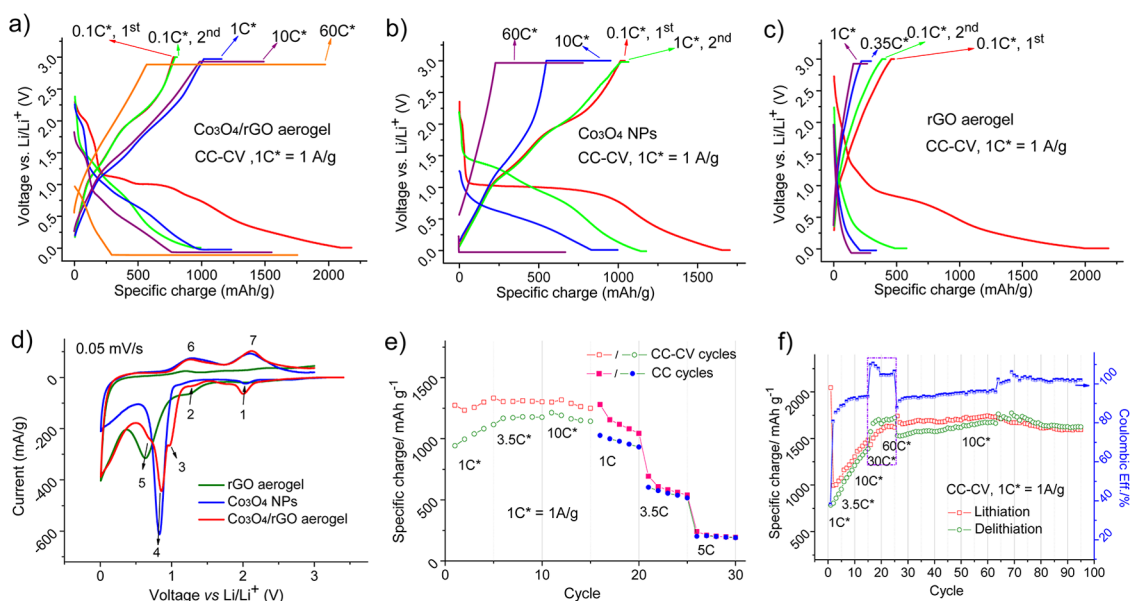
Figure 2. Constant current + constant voltage (CC+CV) cycling profiles for (a) the Co$_3$O$_4$/rGO composite aerogel, (b) the as-obtained Co$_3$O$_4$ NPs with 30% of carbon black and 10% of binder and (c) the rGO aerogel without any NPs. (d) Comparison of the cyclic voltammetry scans for all three samples. (e) Comparison between CC+CV cycles and CC cycles for Co$_3$O$_4$/rGO composite aerogel. (f) Cycle performance of the Co$_3$O$_4$/rGO composite aerogel under CC+CV conditions.

current rates, a CV step might be added after the CC mode on discharge or charge. 1 C* is defined as 1 A g^{-1} through the whole text (* is added if a constant voltage step was applied where the cutoff current was set typically to 0.05 C or higher). To easily compare with the results obtained in other publications, battery performance only under galvanostatic mode is also shown in the figures of composite electrodes.

The results of the CC+CV cycling profiles for the Co$_3$O$_4$/rGO composite aerogel are presented in Figure 2a. On the initial discharge at 0.1 C*, the Co$_3$O$_4$/rGO composite aerogel displays a short plateau at 2.0 V, which could be assigned to the formation of Li$_x$Co$_3$O$_4$.[33] Another plateau at ∼1.2 V comes from the contribution of rGO, as deduced from a comparison of the cyclic voltammetry measurements between all three samples (Figure 2d). Another long plateau at ∼1.0 V results from the conversion reaction of Li$_x$Co$_3$O$_4$ to metallic Co embedded in Li$_2$O.[33,34] Finally, a sloping curve down to the cutoff voltage of 0.01 V develops, which is mainly associated with three processes occurring in parallel: the solid electrolyte interphase (SEI) formation, the reduction of functional groups bound to the graphene oxide layers, and the double side adsorption of Li$^+$ on the graphene oxide layers.[31,35,36] In total, 2184 mAh g^{-1} are delivered. Two oxidation peaks at 1.3 and 2.1 V on the first charge arise from Li$^+$ extraction, transforming the material back to Co$_3$O$_4$/CoO and graphene layers.[34,35,37] A capacity of 792 mAh g^{-1} is covered (Figure 1a, first charge), corresponding to an initial Coulombic efficiency of 36.3%. The low Coulombic efficiency is mainly due to the high surface area, which comes along with the irreversible formation of SEI as well as with the irreversible reaction with

functional groups on graphene oxide layers.[35] The issue of a low initial efficiency can be improved by a prelithiation procedure.[14] After several cycles at 0.1 C*, the composite aerogel seems to be activated, it presents better EC behavior upon each cycle (Figure 1a,f). The total capacity delivered at 1 C* is higher than that obtained at 0.1 C* while the potential hysteresis between charge and discharge is also decreased. Even at 10 C*, the composite Co$_3$O$_4$/rGO aerogel can charge the same capacity on the CC part as the curve at 1 C*. In total, the capacity delivered at 10 C* is 1494 mAh g^{-1}, with 503 mAh g^{-1} contribution from the CV part. At 60 C*, the total capacity further increases to 1963 mAh g^{-1}, but the largest contribution comes from the CV part, namely 1385 mAh g^{-1}. As the current increases to such high rates, the different kinetics in the lithiation and delithiation can be clearly observed: the lithiation process is more sluggish than that of the delithiation, which is also confirmed by the asymmetric cycling tests shown in Figure S10. Nevertheless, even without the help of the CV part, the Co$_3$O$_4$/rGO composite aerogel demonstrates its high rate capability as shown in Figure 2e. It can deliver about 1005 mAh g^{-1} at 1 C, 580 mAh g^{-1} at 3.5 C and 205 mAh g^{-1} at 5 C rate.

An interesting phenomenon is observed for the rate-capability plot: when the current increases from 10 C* to 30/60 C*, the Coulombic efficiency reaches more than 100%, as shown in the purple box in Figure 2f. It seems that the Li$^+$ ions, trapped in the porous electrode during previous cycles, are suddenly released. The same observation could be made on other composite aerogel samples (Figure S6–S8), but never on the conventionally prepared NP or pure rGO samples (Figure 2b,c). Accordingly, it seems that this unusual kinetic behavior

is related to the influence of the hierarchical, porous microstructure on the lithium deposition in the composite aerogels at very high current rates.

For comparison, conventionally prepared electrodes were fabricated from as-obtained Co_3O_4 NPs using 30 wt % of carbon black and 10 wt % of binder (PVDF). Shown in Figure 2b, on the first discharge at 0.1 C* a short potential plateau at 2.0 V is followed by a long plateau at ~1.0 V and a sloping curve down to the cutoff voltage. Overall, 1702 mAh g^{-1} can be delivered. On delithiation at 0.1 C*, two short plateaus appear at ~1.2 and ~2.1 V, respectively, with a total specific charge of 1044 mAh g^{-1}, giving an initial Coulombic efficiency of 61.3%. On the second discharge at 1 C*, the plateau at 1.0 V disappears at the expense of a slope with blurred plateaus extracting a total specific charge of 1180 mAh g^{-1}. In the second cycle, the Coulombic efficiency is enhanced to 90.7%. However, at a rate of 10 C* the hysteresis between charge and discharge is much larger than that of the 1 C* curve, and it is even more pronounced for high rates at 60 C*, where Co_3O_4 NPs show significant overpotentials, leading to a premature hitting of the cut-off potential upon discharge.

As a second reference, the pure rGO aerogel without any embedded NPs was also tested under the same conditions (Figure 2c). The initial discharge capacity of 2186 mAh g^{-1} at 0.1 C* is remarkably high. However, the first delithiation capacity at 0.1 C* is only 481 mAh g^{-1}, which gives an initial Coulombic efficiency of only 22.0%. After the first cycle at 0.1 C*, the total capacities continue dropping upon every cycle. After five cycles at 1 C*, it can merely deliver a capacity of 294 mAh g^{-1} on discharge and 269 mAh g^{-1} on charge. These specific charges are close to those of graphite electrodes, indicating restacking of the rGO sheets to a graphite-like structure.[38] The significantly lower electrochemical performances of these two reference samples clearly emphasize the importance of a rational design of the microstructure of the composite electrode.

To acquire more insight into the exceptional EC behavior of the rGO-based composite aerogels, electrochemical impedance spectroscopy (EIS) measurements at an amplitude of 10 mV over the frequency range from 100 kHz to 0.01 Hz were carried out on the pristine electrodes as well as on the ones that went through different cycles. In Figure 3, we show the Co_3O_4/rGO aerogel as a representative example of all the other samples that display similar results (Figure S6–S9). The pristine electrode does not undergo any charge-transfer reactions and only diffusional processes (Warburg impedance part) take place. However, after three cycles at 0.1 C the response of the electrode changes significantly and a semicircle can be observed, indicating a proper charge transfer reaction. Thus, the composite electrodes become activated as already observed in the total extracted specific charge in Figure 2f and in Figure 5 (see below). Galvanostatic
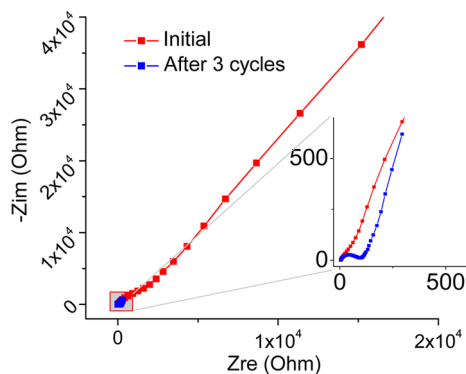

Figure 3. EIS spectra of the Co_3O_4/rGO composite aerogel before and after 3 cycles at 3 V *vs* Li$^+$/Li.

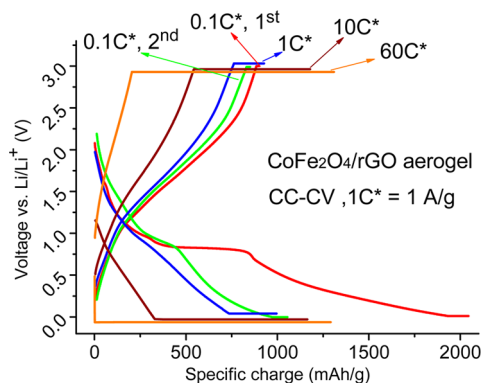**Figure 4.** CC+CV cycling profiles for the $CoFe_2O_4$/rGO composite aerogel at different current rates.

intermittent titration technique (GITT) was applied to the composite Co_3O_4/rGO aerogel as shown in Figure S11. From the GITT, the large voltage hysteresis is clearly visible even at low rates of C/20. Additionally, after 5 h of open-circuit the potential still relaxes. This observation indicates an inhomogeneous reaction of the Co_3O_4 nanocrystals as a result of a core–shell reaction front mechanism typically observed for conversion materials.[39]

To underline the general applicability and benefit of our electrode design with its hierarchical porous microstructure, we discuss, as another sample, the $CoFe_2O_4$/rGO composite fabricated by the same protocol. Figure 4 presents the results of CC+CV cycling profiles. On the initial cycle at 0.1 C*, the $CoFe_2O_4$/rGO aerogel delivers capacities of 2045 mAh g^{-1} on lithiation and 904 mAh g^{-1} on delithiation, corresponding to a Coulombic efficiency of 44.2%. On the second cycle at 0.1 C*, a rapid improvement to 80.6% occurs as a result of 1045 mAh g^{-1} on lithiation and 842 mAh g^{-1} on delithiation. Similar to the results of the Co_3O_4/rGO composite, capacities are accumulated over cycles. For instance, 929, 1177, and 1290 mAh g^{-1} are discharged at current rates of 1, 10, and 60 C*, respectively. To demonstrate the long-term stability, the $CoFe_2O_4$/rGO composite aerogel was galvanostatically cycled without the help of the constant voltage part, and it manifests a
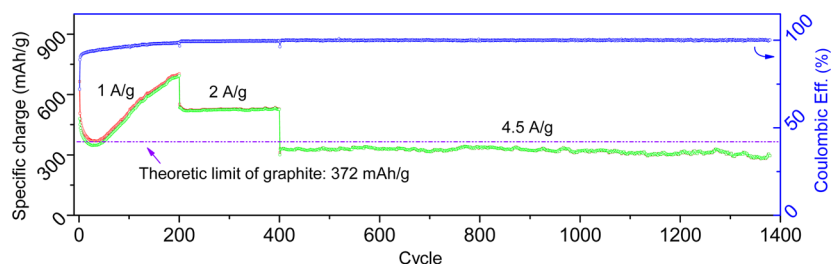
Figure 5. Rate capability and long-term stability performance for the CoFe$_2$O$_4$/rGO composite aerogel under galvanostatic condition without the help of a constant voltage part.

remarkable rate capability and long-lived cycle performance. As shown in Figure 5, at 1 A g^{-1}, it goes through a capacity fading down to 360 mAh g^{-1} in the first 30 cycles. In the following 170 cycles, the composite electrode is activated and the capacity gradually increases back to 700 mAh g^{-1}. The average Coulombic efficiency for the first 200 cycles at 1 A g^{-1} is 96.2%. For the next 200 cycles the current rate is increased to 2 A g^{-1}. Nevertheless, the electrode still delivers a very stable capacity of around 520 mAh g^{-1} with an average efficiency of 99.6%. To test the limit of the electrode, the current rate was further promoted to 4.5 A g^{-1} for another 1000 cycles with the result that the CoFe$_2$O$_4$/rGO composite aerogel still gives an impressive capacity of around 330 mAh g^{-1}, approaching the theoretic limit of graphite (372 mAh g^{-1}). The average Coulombic efficiency on these 1000 cycles is close to 100%.

CONCLUSION

In summary, using colloidally stable spinel-type NPs and GO as building blocks with their tailored surface charges, we developed a facile method to fabricate flexible composite spinel-type metal oxide/rGO aerogels with any desired shape that can directly be used as binder-free anodes in LIBs. Benefiting from several structural features provided by this carefully designed electrode architecture, including hierarchical porosity, conductive network and mechanical stability offered by the interpenetrated rGO layers, and the pillar effect of NPs in between the rGO sheets, the hybrid system synergistically enhances the intrinsic properties of each component. Consequently, the spinel/rGO composite aerogel demonstrates much enhanced rate capability and long-term stability without obvious capacity fading after 1000 cycles at high rates. We believe that the strategy presented here can be extended to other metal oxides, sulfides, and alloys (*e.g.*, Ge or Sn) for the preparation of advanced anodes in LIBs. In addition, the hierarchically porous microstructure in such hybrids is promising for other applications, *e.g.*, in supercapacitors or in catalysis.

EXPERIMENTAL SECTION

Chemicals. Co(II) acetate (99.995%), Fe(III) acetylacetonate (99.9%), Co(II) acetylacetonate (97%), Ni(II) acetate tetrahydrate (99.998%), Mn(II) acetate (98%), benzyl alcohol (BnOH, 99.8%), ethylenediamine (EDA, 99%), aqueous ammonia solution (~25%) and 2-[2-(2-methoxyethoxy)ethoxy]acetic acid (MEEAA, 99%) were purchased from Sigma-Aldrich and used as received without further purification. Graphene oxide (2.5−10 mg/mL in H$_2$O, GO) was purchased from Royal Elite (Shanghai).

Oil Bath Synthesis of Co$_3$O$_4$ NPs. 1 mmol Co(II) acetate was dissolved into 7 mL of BnOH under stirring. After several minutes, 7 mL of ammonia solution was added into the open vessel. The reddish emulsion was put into an oil bath set at 165 °C, upon which it started to boil immediately with substantial bubble evolution. After ~5 min, a reddish solution with significantly reduced volume was obtained, which was kept at 165 °C for 2 h under continuous stirring, leading to a black suspension. The black precipitate was harvested by adding diethyl ether before centrifugation, washed twice with ethanol, and finally dried in an oven at 60 °C. The dry powder was dispersed into H$_2$O with different concentrations from 10 to 30 mg/mL simply by shaking and sonication (1 min), which turned out to produce colloidal solutions stable for several weeks.

Microwave-Assisted Synthesis of MFe$_2$O$_4$. For the synthesis of Fe$_3$O$_4$, 1 mmol of Fe(III) acetylacetonate and 100 μL of EDA were added into 5 mL of benzyl alcohol in a 10 mL microwave glass tube in an Ar-filled glovebox and stirred for 20 min. The reaction mixture was heated under microwave irradiation at 195 °C for 10 min. The resulting product was washed with diethyl ether once and with a 1:1 mixture of ethanol and diethyl ether for another three times. The obtained wet precipitate was then dispersed in H$_2$O containing MEEAA (10 μL/ml). The mixture (20−30 mg/mL NPs) was sonicated for 1 h, resulting in a colloidally stable dispersion. For the synthesis of the other spinels MFe$_2$O$_4$ (M = Co, Mn, Ni), 0.5 mmol Fe(III) acetylacetonate with 0.25 mmol of Mn(II) acetate, Co(II) acetylacetonate or Ni(II) acetate tetrahydrate, respectively, were dissolved in 5 mL of benzyl alcohol with addition of 100 μL of EDA. All other experimental conditions were the same as for the Fe$_3$O$_4$ synthesis.

Fabrication of Spinel/rGO Composite Aerogel. The GO (5 mg/mL, typically) and the NP dispersion (20 mg/mL, typically) were homogeneously mixed under sonication (5−10 min). The weight percent of NPs was typically kept at 70%. However, other NP loadings (up to 90 wt %) could be produced by varying the relative concentrations of NPs and GO (Figure S12). The mixed suspension was transferred onto a Petri-dish like current collector (made of Cu, Ti or Al) or another container, sealed in a closed bottle, and cured under a saturated H$_2$O vapor environment at 95 °C for 6 h. A monolithic gel film formed without obvious volume shrinkage. The gel was carefully put into an excess of acetone for solvent exchange twice (24 h), followed by drying in supercritical CO$_2$. A monolithic, crack-free aerogel film with minimum thickness of ~100 μm was finally obtained. A free-standing film with some extent of volume shrinkage could also be produced if other containers were used (*e.g.*, Teflon).

Electrode Preparation. The as-obtained composite aerogel film on a Ti current collector was additionally vacuum-dried at 100 °C and later on directly used as electrode without any additives. To investigate the annealing effect on graphene oxide, the composite aerogel was either heated to 250 °C or to 280 °C in N_2 plus 5 vol % H_2 for 6 h with a ramping rate of 2 °C/min (Figure S13–S14). For comparison, Co_3O_4 electrodes were prepared in a conventional way, i.e., 60 wt % of Co_3O_4 was uniformly mixed with 30 wt % of carbon black (Super P, TIMCAL), 10 wt % of PVDF (polyvinylidene fluoride, Aldrich) in NMP (N-methyl-2-pyrrolidinone, Fluka) under mechanical stirring. The resulting paste was transferred onto a Ti current collector and vacuum-dried at 100 °C overnight. The average electrode loading was $1-1.5$ mg/cm^2. Higher loadings could also be achieved using larger concentrations of GO and NP suspensions.

Electrochemical Measurements. Electrodes were assembled into Swagelok-type cells in an Ar-filled glovebox ($H_2O, O_2 < 0.1$ ppm). Li metal (99.9%, Alfa-Aesar) served as both reference and counter electrode. A glass fiber separator was soaked with electrolyte (1 M $LiPF_6$ in 1:1 wt % ethylene carbonate (EC)/dimethyl carbonate (DMC), Novolyte). All electrochemical measurements were performed using a Biologic instrument (VMP3) at room temperature. The electrodes were cycled between 0.01 and 3 V vs Li/Li$^+$ for varying specific current rates. 1 C was defined as 1 A g^{-1}. If a constant voltage step was added, the cutoff current was set at 0.05 A g^{-1}.

Characterizations. X-ray powder diffraction (XRD) patterns were recorded using a PANalytical diffractometer (Empyrean with monochromator, Cu Kα radiation). The morphologies were studied by a LEO 1530 Gemini scanning electron microscope (SEM) working at 5 kV and by a Philips CM 12 transmission electron microscope (TEM) at 100 kV. The ζ-potential information was obtained on Zeta Potential Analyzer (DelsaNano C, Beckman Coulter). X-ray photoelectron spectra (XPS) were recorded on a Sigma 2 spectrometer (Thermo scientific) using a polychromatic Al Kα X-ray source, where binding energy was calibrated taking C 1s = 285.0 eV. Nitrogen adsorption/desorption isotherms were measured on a Quantachrome Autosorb-iQ to acquire the specific surface area and pore size distribution by the BET and DFT method, respectively. The carbon contents were determined by thermogravimetric analysis (TGA, Q500, TA Instruments).

REFERENCES AND NOTES

1. Tarascon, J. M.; Armand, M. Issues and Challenges Facing Rechargeable Lithium Batteries. *Nature* **2001**, *414*, 359–367.
2. Goodenough, J. B. Evolution of Strategies for Modern Rechargeable Batteries. *Acc. Chem. Res.* **2013**, *46*, 1053–1061.
3. Li, N.; Chen, Z.; Ren, W.; Li, F.; Cheng, H.-M. Flexible Graphene-Based Lithium Ion Batteries with Ultrafast Charge and Discharge Rates. *Proc. Natl. Acad. Sci. U. S. A.* **2012**, *109*, 17360–17365.
4. Zhou, F.; Xin, S.; Liang, H.-W.; Song, L.-T.; Yu, S.-H. Carbon Nanofibers Decorated with Molybdenum Disulfide Nanosheets: Synergistic Lithium Storage and Enhanced Electrochemical Performance. *Angew. Chem., Int. Ed.* **2014**, *53*, 11552–11556.
5. Chang, K.; Chen, W. L-Cysteine-Assisted Synthesis of Layered MoS₂/Graphene Composites with Excellent Electrochemical Performances for Lithium Ion Batteries. *ACS Nano* **2011**, *5*, 4720–4728.
6. Kim, Y.; Lee, J.-H.; Cho, S.; Kwon, Y.; In, I.; Lee, J.; You, N.-H.; Reichmanis, E.; Ko, H.; Lee, K.-T.; *et al.* Additive-Free Hollow-Structured Co_3O_4 Nanoparticle Li-Ion Battery: The Origins of Irreversible Capacity Loss. *ACS Nano* **2014**, *8*, 6701–6712.
7. Wu, Z.-S.; Ren, W.; Wen, L.; Gao, L.; Zhao, J.; Chen, Z.; Zhou, G.; Li, F.; Cheng, H.-M. Graphene Anchored with Co_3O_4 Nanoparticles as Anode of Lithium Ion Batteries with Enhanced Reversible Capacity and Cyclic Performance. *ACS Nano* **2010**, *4*, 3187–3194.
8. Jiang, J.; Li, Y.; Liu, J.; Huang, X.; Yuan, C.; Lou, X. W. Recent Advances in Metal Oxide-Based Electrode Architecture Design for Electrochemical Energy Storage. *Adv. Mater.* **2012**, *24*, 5166–5180.
9. Bruce, P. G.; Scrosati, B.; Tarascon, J.-M. Nanomaterials for Rechargeable Lithium Batteries. *Angew. Chem., Int. Ed.* **2008**, *47*, 2930–2946.
10. Wu, F.; Ma, X.; Feng, J.; Qian, Y.; Xiong, S. 3D Co_3O_4 and CoO@C Wall Arrays: Morphology Control, Formation Mechanism, and Lithium-Storage Properties. *J. Mater. Chem. A* **2014**, *2*, 11597–11605.
11. Li, B.; Cao, H.; Shao, J.; Li, G.; Qu, M.; Yin, G. Co_3O_4@ graphene Composites as Anode Materials for High-Performance Lithium Ion Batteries. *Inorg. Chem.* **2011**, *50*, 1628–1632.
12. Wang, Y.; Xia, H.; Lu, L.; Lin, J. Excellent Performance in Lithium-Ion Battery Anodes: Rational Synthesis of Co-$(CO_3)_{0.5}(OH)_{0.11}H_2O$ Nanobelt Array and Its Conversion into Mesoporous and Single-Crystal Co_3O_4. *ACS Nano* **2010**, *4*, 1425–1432.
13. Huang, G.; Xu, S.; Lu, S.; Li, L.; Sun, H. Micro-/Nanostructured Co_3O_4 Anode with Enhanced Rate Capability for Lithium-Ion Batteries. *ACS Appl. Mater. Interfaces* **2014**, *6*, 7236–7243.
14. Liu, N.; Lu, Z.; Zhao, J.; McDowell, M. T.; Lee, H. W.; Zhao, W.; Cui, Y. A Pomegranate-Inspired Nanoscale Design for Large-Volume-Change Lithium Battery Anodes. *Nat. Nanotechnol.* **2014**, *9*, 187–92.
15. Kwon, Y. H.; Woo, S.-W.; Jung, H.-R.; Yu, H. K.; Kim, K.; Oh, B. H.; Ahn, S.; Lee, S.-Y.; Song, S.-W.; Cho, J.; Shin, H.-C.; Kim, J. Y. Cable-Type Flexible Lithium Ion Battery Based on Hollow Multi-Helix Electrodes. *Adv. Mater.* **2012**, *24*, 5192–5197.
16. Zhai, Y.; Dou, Y.; Zhao, D.; Fulvio, P. F.; Mayes, R. T.; Dai, S. Carbon Materials for Chemical Capacitive Energy Storage. *Adv. Mater.* **2011**, *23*, 4828–4850.
17. Xin, S.; Guo, Y.-G.; Wan, L.-J. Nanocarbon Networks for Advanced Rechargeable Lithium Batteries. *Acc. Chem. Res.* **2012**, *45*, 1759–1769.
18. Roberts, A. D.; Li, X.; Zhang, H. Porous Carbon Spheres and Monoliths: Morphology Control, Pore Size Tuning and Their Applications as Li-Ion Battery Anode Materials. *Chem. Soc. Rev.* **2014**, *43*, 4341–4356.
19. Antonietti, M.; Fechler, N.; Fellinger, T.-P. Carbon Aerogels and Monoliths: Control of Porosity and Nanoarchitecture *via* Sol−Gel Routes. *Chem. Mater.* **2013**, *26*, 196–210.
20. Heiligtag, F. J.; Rossell, M. D.; Süess, M. J.; Niederberger, M. Template-Free Co-Assembly of Preformed Au and TiO_2 Nanoparticles into Multicomponent 3D Aerogels. *J. Mater. Chem.* **2011**, *21*, 16893–16899.
21. Rechberger, F.; Heiligtag, F. J.; Süess, M. J.; Niederberger, M. Assembly of $BaTiO_3$ Nanocrystals into Macroscopic Aerogel Monoliths with High Surface Area. *Angew. Chem., Int. Ed.* **2014**, *53*, 6823–6826.
22. Heiligtag, F. J.; Airaghi Leccardi, M. J. I.; Erdem, D.; Süess, M. J.; Niederberger, M. Anisotropically Structured Magnetic Aerogel Monoliths. *Nanoscale* **2014**, *6*, 13213–13221.

23. Wang, L.; Zhuo, L.; Zhang, C.; Zhao, F. Embedding $NiCo_2O_4$ Nanoparticles into a 3DHPC Assisted by CO_2-Expanded Ethanol: A Potential Lithium-Ion Battery Anode with High Performance. *ACS Appl. Mater. Interfaces* **2014**, *6*, 10813–10820.

24. Yin, L.; Zhang, Z.; Li, Z.; Hao, F.; Li, Q.; Wang, C.; Fan, R.; Qi, Y. Spinel $ZnMn_2O_4$ Nanocrystal-Anchored 3D Hierarchical Carbon Aerogel Hybrids as Anode Materials for Lithium Ion Batteries. *Adv. Funct. Mater.* **2014**, *24*, 4176–4185.

25. Yang, S.; Feng, X.; Ivanovici, S.; Müllen, K. Fabrication of Graphene-Encapsulated Oxide Nanoparticles: Towards High-Performance Anode Materials for Lithium Storage. *Angew. Chem., Int. Ed.* **2010**, *49*, 8408–8411.

26. Zhu, J.; Zhu, T.; Zhou, X.; Zhang, Y.; Lou, X. W.; Chen, X.; Zhang, H.; Hng, H. H.; Yan, Q. Facile Synthesis of Metal Oxide/Reduced Graphene Oxide Hybrids with High Lithium Storage Capacity and Stable Cyclability. *Nanoscale* **2011**, *3*, 1084–1089.

27. Bilecka, I.; Kubli, M.; Amstad, E.; Niederberger, M. Simultaneous Formation of Ferrite Nanocrystals and Deposition of Thin Films *via* a Microwave-Assisted Nonaqueous Sol−Gel Process. *J. Sol-Gel Sci. Technol.* **2011**, *57*, 313–322.

28. Adhikari, B.; Biswas, A.; Banerjee, A. Graphene Oxide-Based Hydrogels to Make Metal Nanoparticle-Containing Reduced Graphene Oxide-Based Functional Hybrid Hydrogels. *ACS Appl. Mater. Interfaces* **2012**, *4*, 5472–5482.

29. Hu, H.; Zhao, Z.; Wan, W.; Gogotsi, Y.; Qiu, J. Ultralight and Highly Compressible Graphene Aerogels. *Adv. Mater.* **2013**, *25*, 2219–23.

30. Cong, H.-P.; Chen, J.-F.; Yu, S.-H. Graphene-Based Macroscopic Assemblies and Architectures: An Emerging Material System. *Chem. Soc. Rev.* **2014**, *43*, 7295–7325.

31. Sun, Y.; Wu, Q.; Shi, G. Graphene Based New Energy Materials. *Energy Environ. Sci.* **2011**, *4*, 1113–1132.

32. Wu, Z.-S.; Sun, Y.; Tan, Y.-Z.; Yang, S.; Feng, X.; Müllen, K. Three-Dimensional Graphene-Based Macro- and Mesoporous Frameworks for High-Performance Electrochemical Capacitive Energy Storage. *J. Am. Chem. Soc.* **2012**, *134*, 19532–19535.

33. Pralong, V.; Leriche, J. B.; Beaudoin, B.; Naudin, E.; Morcrette, M.; Tarascon, J. M. Electrochemical Study of Nanometer Co_3O_4, Co, $CoSb_3$ and Sb Thin Films Toward Lithium. *Solid State Ionics* **2004**, *166*, 295–305.

34. Kang, Y. M.; Song, M. S.; Kim, J. H.; Kim, H. S.; Park, M. S.; Lee, J. Y.; Liu, H. K.; Dou, S. X. A Study on the Charge-Discharge Mechanism of Co_3O_4 as an Anode for the Li Ion Secondary Battery. *Electrochim. Acta* **2005**, *50*, 3667–3673.

35. Pan, D.; Wang, S.; Zhao, B.; Wu, M.; Zhang, H.; Wang, Y.; Jiao, Z. Li Storage Properties of Disordered Graphene Nanosheets. *Chem. Mater.* **2009**, *21*, 3136–3142.

36. Memarzadeh Lotfabad, E.; Kalisvaart, P.; Kohandehghan, A.; Karpuzov, D.; Mitlin, D. Origin of Non-SEI Related Coulombic Efficiency Loss in Carbons Tested against Na and Li. *J. Mater. Chem. A* **2014**, *2*, 19685–19695.

37. Su, Q.; Zhang, J.; Wu, Y.; Du, G. Revealing the Electrochemical Conversion Mechanism of Porous Co_3O_4 Nanoplates in Lithium Ion Battery by *In Situ* Transmission Electron Microscopy. *Nano Energy* **2014**, *9*, 264–272.

38. Yoo, E.; Kim, J.; Hosono, E.; Zhou, H.-s.; Kudo, T.; Honma, I. Large Reversible Li Storage of Graphene Nanosheet Families for Use in Rechargeable Lithium Ion Batteries. *Nano Lett.* **2008**, *8*, 2277–2282.

39. Ebner, M.; Marone, F.; Stampanoni, M.; Wood, V. Visualization and Quantification of Electrochemical and Mechanical Degradation in Li Ion Batteries. *Science* **2013**, *342*, 716–720.